

Modeling Transit Time Distributions in Microvascular Networks

Nathaniel J. Karst^a, John B. Geddes^b

^a*Babson College, Wellesley, 02457, MA, USA*

^b*Olin College of Engineering, Needham, 02492, MA, USA*

Abstract

The time a red blood cell (RBC) spends in the microvasculature is of prime importance for a number of physiological processes. In this work, present a novel methodology for computing an approximation of the so-called transit time distribution (TTD), i.e., the probabilistic description of how long a RBC will reside within the network. As a proof of concept, we apply this methodology to two flavors of the honeycomb network. We show that each network type supports a wealth of distinct steady-state configurations and we present tools for analyzing the associated collection of TTDs, ranging from standard measures like mean capillary transit time (MCTT) and capillary transit time heterogeneity (CTTH) to novel metrics.

1. Introduction

The time a cells spend traversing through micro-vascular networks is of critical importance to a number of physiological processes. At the level of a single capillary, the potential for a red blood cell (RBC) to supply oxygen is determined primarily by its transit time $\tau = V/Q$, where V is the volume of the vessel and Q is the volumetric flow rate through the vessel [1]. If the flow rate is small, then τ is large, and RBCs remain in the capillary well after they have exchanged their available oxygen. Moreover, few fresh RBCs are entering the capillary to replace these depleted cells, and thus overall oxygen exchange along the vessel is minimal. As flow rate initially increases, transit time decreases rapidly. RBCs can be shuttled through the capillary

Email address: `nkarst@babson.edu` (Nathaniel J. Karst)

without being depleted of oxygen, and overall oxygen exchange along the vessel rises significantly. As Q continues to increase, transit times fall less and less quickly – there are clear diminishing returns given the functional form of τ – and the change in overall oxygen exchange slows in kind.

While helpful for a conceptual framing, this single capillary view necessarily misses the larger story: RBCs travel along complex pathways composed of the concatenation of individual capillaries as they move through the microvasculature. Even at steady-state, the transit times of different RBCs in the same network can be quite different, due to both the diversity of these pathways and the wide ranges of flow rates experienced in individual vessels. The *transit time distribution* (TTD) of a given network in a particular steady-state configuration is the probability density function (PDF) describing the proportion of RBCs entering the network at time t that will exit the network at time $t + \tau$. The first and second moments of the TTD, *mean capillary transit time* and *capillary transit time heterogeneity*, respectively, have received significant attention in the literature.

Given that the transit time in individual capillaries determines overall oxygen exchange, mean capillary transit time (MCTT) gives one metric for the “typical” oxygenation potential of a RBC over its entire transit through the network. Note that this is just one possible formulation. We might also consider the bulk transit time, that is, total network volume divided by total incoming volumetric flow, or median transit time, so that very long delay flow pathways carrying a very small proportion of the overall RBCs in the network do not unduly affect our metric. In our work here, we will focus primarily on MCTT as our preferred measure of central tendency.

Capillary transit time heterogeneity (CTTH) is a critical measure that characterizes the health of a network. Jespersen et al [2] report that CTTH plays a critical role in tissue oxygenation and that disturbing the CTTH may adversely affect cerebral oxygen metabolism. Using a realistic network, Goirand et. al [3] use simulations based on experimental data to explore the transit time dynamics in the network. They find scaling laws of transit time distributions consistent with a simple stochastic model, and show that regions of low flow can occur, which may play an important role in brain disease.

Ischemic heart disease often involves a deficiency in oxygen supply, and Østergaard et al [4] have provided evidence that increases in the capillary transit time heterogeneity are due to shunts for oxygenated blood that leaves regions of the tissue bed starved for oxygen, resulting in tissue hypoxia and

angina. Reduction in oxygen supply to tissues often occurs in diseases like diabetes and aging, and Lücker et al [5, 6] have shown that the CTTH is strongly correlated with the hemoglobin saturation drop across a microvascular network.

An assumption common to many of these works is that the transit time of cells is governed by a *unique* equilibrium distribution of flow and hematocrit through a network. However, computing flow (and hematocrit) in a microvascular network is challenging because it is a nonlinear network flow problem—see [7] for general examples of nonlinear network flow problems. We have shown that multiple equilibrium states are possible [8, 9], and confirmed these predictions in a model fluid system [10]. Although not of interest here, the stability picture is also complicated and nonlinear oscillations in flow and hematocrit may exist, even when all network parameters and boundary conditions are fixed [11, 12, 13, 14, 15, 16, 17, 18, 19].

In this work, we propose a mechanistic model for capillary TTDs in arbitrary microvascular networks that requires neither detailed particle-tracking simulation of network flow nor analytic assumptions about volumetric flow rate distributions. This model is based on a simple Markovian assumption that can be refined for increasingly precise description of the TTD. The Markovian nature of this assumption is identical in spirit to Huang et al [20], but their work relies on a connectivity matrix based on the modified Horsfield’s Strahler index method presented by Huang et al [21]. Here, our equivalent “connectivity matrix” encodes the fine grain probabilistic information about flow pathways via the incidence matrix of the underlying graph and preferential routing of RBCs at diverging bifurcations, rather than the coarse grain structural information about the network via the Strahler index.

As an example use case for this methodology, we construct two honeycomb-type networks which have been used extensively to model various tissue types [22, 23, 24, 25]. Theory suggests the networks should support many different steady-state configurations. We present a framework for calculating a TTD for each distinct equilibrium and investigate this collection of TTDs using both traditional tools like MCTT and CTTH, as well as novel metrics designed to leverage the wealth of TTDs supported by a single network.

2. Methods

In this section, we first lay out of methodology for network specification and our choices for constitutive laws like viscosity and plasma-skimming. We

next present a refined and highly generalized description of the governing equations of blood flow in these model microvascular network and propose an approach that significantly reduces the dimensionality of the nonlinear problem. We then discuss the derivation of the TTD itself from the system's steady-state flow and hematocrit profiles. As a prelude to our main experiments, we examine a small model network. We show the manual construction of a single TTD, and then compare the TTDs of all 9 of the equilibria supported by the network. Finally, we outline our main experiments: the construction and analysis of hundreds of TTDs for two medium-sized honeycomb networks.

2.1. Network Specification and Boundary Conditions

Any network specification must dictate both incidence, the manner in which nodes (N_n in total) in the network are connected by vessels (N_v in total), and geometry, the lengths and diameters of the vessels themselves. We see a set of example networks in Figure 5. We assume that all nodes in the network can be divided into exterior nodes that have degree one (that is, have only one associated vessel, indicated by black marker color in Figure 5) and interior nodes that have degree three (indicated by white marker color in Figure 5). We define the flow between two nodes to have positive sign if the fluid proceeds from the smaller index node to the larger index node and vice versa for negative flows [11], and we formulate the $N_n \times N_v$ incidence matrix \mathbf{J} of the network with respect to this sign convention; each row of \mathbf{J} represents a node, each column of \mathbf{J} represents a vessel, and the column corresponding to vessel (i, j) , $i < j$, contains -1 in row i , contains +1 in row j , and contains 0 in all other rows. As we will show, this single matrix will be sufficient for capturing most steady-state flow constraints.

2.2. Constitutive Laws

The viscosity of blood is a nonlinear function of both hematocrit and vessel diameter, and various authors have built empirical models to capture the so-called Fåhræus-Lindqvist effect with precision [26]. For simplicity, here we use a one parameter Arrhenius-type viscosity law,

$$\mu(H) = e^{\delta H}, \quad (1)$$

where μ is the relative viscosity of blood (to plasma), H is the hematocrit, and δ is a viscosity parameter. Average human hematocrit is roughly 0.45,

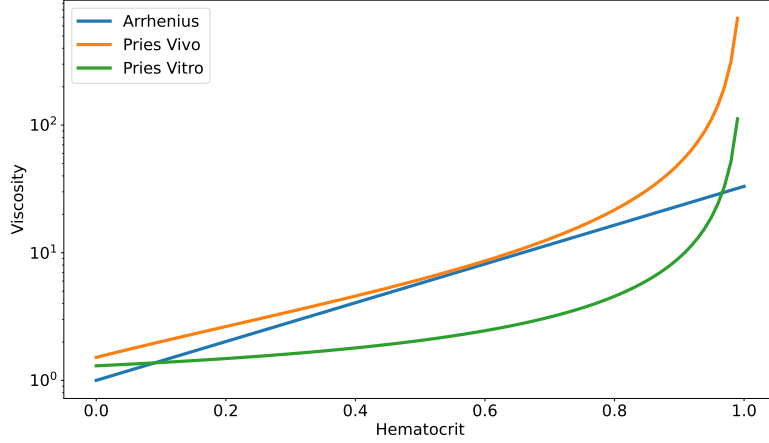


Figure 1: Comparison of Arrhenius viscosity law (Equation 1) with $\delta = 3.58$ to Pries *in vivo* and *in vitro* skimming function with $d = 15 \mu\text{m}$.

and the relative blood viscosity in small diameter vessels is approximately 5 [26]. A typical value of our viscosity parameter is therefore $\delta = 3.58$. Figure 1 shows a comparison of several commonly used viscosity laws.

The differential distribution of plasma and RBCs at diverging vessel junctions – an effect known as plasma skimming – depends on a number of physiological factors, including the diameters of the daughter vessels, the angle between the daughter vessels and the parent vessel, the flow rates in the daughter vessels relative to the feed vessel, and the hematocrit in the feed vessel [27]. Rather than modeling changes in RBC volumes directly, most models instead capture changes in hematocrit between feed vessel F and daughter vessels A and B . In principle, so-called plasma skimming models can include any or all of the factors listed above. In practice, many models take a more parametric approach, including the formulation we adopt here [28]:

$$H_A - H_F \left(\frac{Q^{p-1}}{Q^p + (1 - Q)^p} \right) = 0 \quad (2)$$

where $Q = Q_A/Q_F$ is the relative proportion of total feed flow diverted to daughter vessel A . The skimming parameter p captures the strength of the plasma skimming effect: with $p = 1$, there is no differential distribution of RBCs due to differences in flow rates in the daughter vessels, but RBCs are

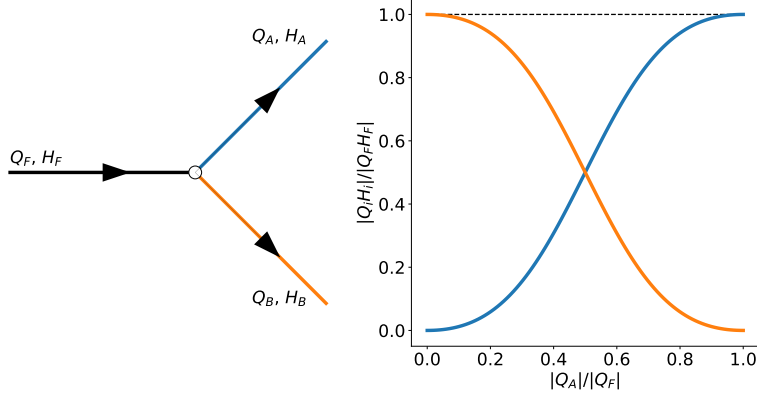


Figure 2: Schematic of diverging junction (left pane) in which RBC fraction in daughter vessels A and B are determined by Klitzman-Johnson plasma skimming with $p = 2$ (right pane).

preferential routed to the daughter vessel with higher flow as p increases. This plasma skimming model is implemented at all diverging nodes; see Figure 2.

In vessels with small diameters, RBCs tend to be more plentiful near the axial center, where the bulk fluid velocity is largest, and less plentiful near the vessel walls, where bulk fluid velocity is smallest. Together, these lead to so-called Fåhræus effect, that is, a discrepancy between the *tube hematocrit*, the area-weighted RBC concentration that one would observe in the vessel, and the *discharge hematocrit*, the RBC concentration one would observe in a discharge reservoir. We have explored this effect in previous work and found that including it does not change the nature of the results, only the details [9], and so we disregard it here.

2.3. Equilibrium Identification

The state of the network is specified by a collection of pressures $\mathbf{p} = [P_1, P_2, \dots, P_{N_n}]^T$, flows $\mathbf{q} = [Q_1, Q_2, \dots, Q_{N_v}]^T$, and hematocrits $\mathbf{h} = [H_1, H_2, \dots, H_{N_v}]^T$, giving a total of $N_n + 2N_v$ degrees of freedom.

Recalling that $Q_{i,j}$, $i < j$, is defined by to be positive if flow proceeds from node i to node j , flow balance at each interior node i is expressed as

$$\sum_{j \in N(i), i > j} Q_{i,j} - \sum_{j \in N(i), i < j} Q_{i,j} = 0, \quad (3)$$

where $N(i)$ is the set of nodes adjacent to node i . Poiseuille's law relates the flow $Q_{i,j} = Q_v$ in vessel v that is incident to node i and j , $i < j$, to the pressures P_i and P_j at nodes i and j respectively,

$$Q_v R_v + (P_j - P_i) = 0, \quad (4)$$

where $R_v = 128\mu_v L_v / \pi D_v^4$ is the hydraulic resistance to flow in vessel v . Here, L_v and D_v are the length and diameter of vessel v , respectively, and μ_v is the relative viscosity of blood as dictated by Equation 1.

Both of these constraints can be re-written more succinctly using the network's incidence matrix. For conservation of flow, we have

$$\mathbf{J}_{int} \mathbf{q} = \mathbf{0}, \quad (5)$$

where \mathbf{J}_{int} is the incidence matrix row-restricted to interior nodes. For Poiseuille's law, we have

$$\text{diag}(\mathbf{r}(\mathbf{h})) \mathbf{q} + \mathbf{J}^T \mathbf{p} = \mathbf{0}. \quad (6)$$

Note that the vector of resistances $\mathbf{r}(\mathbf{h})$ is a nonlinear function of the hematocrits \mathbf{h} and that the system is linear in \mathbf{q} and \mathbf{p} once \mathbf{h} is specified.

Similar to conservation of flow, conservation of RBCs at all interior nodes can be expressed in terms of the network incidence matrix,

$$\mathbf{J}_{int} \text{diag}(\mathbf{q}) \mathbf{h} = \mathbf{0}. \quad (7)$$

Note that the roles of \mathbf{q} and \mathbf{h} could be reversed in this formulation; our choice here is arbitrary.

In addition to the RBC conservation constraints from Equation 7, we obtain one additional constraint describing plasma skimming at each diverging node as dictated by Equation 2:

$$\mathbf{S}(\mathbf{q}) \mathbf{h} = \mathbf{0}. \quad (8)$$

Finally, we specify either a pressure *or* flow boundary condition at each exterior node and hematocrit boundary conditions at each inlet nodes:

$$\begin{bmatrix} \mathbf{P}_{ext} & \mathbf{Q}_{ext} \end{bmatrix} \begin{bmatrix} \mathbf{p} \\ \mathbf{q} \end{bmatrix} = \begin{bmatrix} \mathbf{p}_{ext} \\ \mathbf{q}_{ext} \end{bmatrix} \quad (9)$$

$$\mathbf{H}_{ext} \mathbf{h} = \mathbf{h}_{ext}. \quad (10)$$

Note that the matrices in Equation 9 and Equation 10 have a unique entry equal to 1 in each row corresponding to the associated boundary condition and are otherwise zero. Note that the vectors on the right hand side contain only the pressures, flows, and hematocrit values associated with the boundary conditions.

Simultaneous solutions to Equations (5) – (10) represent equilibrium flow, pressure, and hematocrit profiles everywhere in the network. These equations form a nonlinear system, which can be written in the form

$$\mathbf{A}(\mathbf{x})\mathbf{x} = \mathbf{b}, \quad (11)$$

where the matrix \mathbf{A} depends explicitly on the network state variables, $\mathbf{x} = [\mathbf{p} \ \mathbf{q} \ \mathbf{h}]^T$. The known vector \mathbf{b} is all zero except for the boundary pressures, flows, and hematocrits. The matrix \mathbf{A} therefore has block-structure which allows us to decompose the equations:

$$\left[\begin{array}{c|c} \mathbf{B}(\mathbf{h}) & \mathbf{0} \\ \hline \mathbf{0} & \mathbf{C}(\mathbf{q}) \end{array} \right] \begin{bmatrix} \mathbf{p} \\ \mathbf{q} \\ \mathbf{h} \end{bmatrix} = \begin{bmatrix} \mathbf{b}_p \\ \mathbf{b}_q \\ \mathbf{b}_h \end{bmatrix} \quad (12)$$

The $(N_n + N_v) \times (N_n + N_v)$ matrix \mathbf{B} encodes flow balance, Poiseuille's law, and pressure-flow boundary conditions:

$$\mathbf{B}(\mathbf{h}) = \begin{bmatrix} \mathbf{J}^T & \text{diag}(\mathbf{r}(\mathbf{h})) \\ \mathbf{0} & \mathbf{J}_{int} \\ \mathbf{P}_{ext} & \mathbf{Q}_{ext} \end{bmatrix}. \quad (13)$$

The $N_v \times N_v$ matrix \mathbf{C} encodes red cell balance, plasma skimming, and hematocrit boundary conditions:

$$\mathbf{C} \left(\begin{bmatrix} \mathbf{p} \\ \mathbf{q} \end{bmatrix} \right) = \begin{bmatrix} \mathbf{J}_{int} \text{diag}(\mathbf{q}) \\ \mathbf{S}(\mathbf{q}) \\ \mathbf{H}_{ext} \end{bmatrix}. \quad (14)$$

We use this formulation to define the nonlinear functions $\phi : \mathbf{R}^{N_v} \rightarrow \mathbf{R}^{N_n+N_v}$ and $\psi : \mathbf{R}^{N_v} \rightarrow \mathbf{R}^{N_v}$:

$$\phi(\mathbf{h}) = \mathbf{B}(\mathbf{h})^{-1} \begin{bmatrix} \mathbf{b}_p \\ \mathbf{b}_q \end{bmatrix} \quad (15)$$

$$\psi(\mathbf{h}) = \mathbf{h} - \mathbf{C}(\phi(\mathbf{h}))^{-1} \mathbf{b}_h. \quad (16)$$

A hematocrit profile \mathbf{h}^* will lead to an overall pressure-flow-hematocrit equilibrium configuration of the network if and only if $\psi(\mathbf{h}^*) = \mathbf{0}$.

2.4. Transit Time Distribution Computation

Consider a flow pathway comprised of vessels v_1, v_2, \dots, v_n , where v_1 and v_n are any inlet and any outlet of the network, respectively. Without loss of generality, the probability of a RBC traveling along this path is given by the chain rule:

$$\mathbb{P}(v_1, v_2, \dots, v_n) = \mathbb{P}(v_1) \mathbb{P}(v_2 \mid v_1) \cdots \mathbb{P}(v_n \mid v_{n-1}, \dots, v_1) \quad (17)$$

Here, the conditionals should be interpreted as the probability a RBC passes through v_i given it has previously transited v_1, v_2, \dots, v_{i-1} . In practice, estimating the highly conditioned terms towards the right of Eq. 17 would require a detailed spatial understanding of plasma skimming for various feed hematocrits and bifurcation geometries. To make progress, we enforce a local Markov property,

$$\mathbb{P}(v_{i+1} \mid v_i, v_{i-1}, \dots, v_1) = \mathbb{P}(v_{i+1} \mid v_i). \quad (18)$$

Conceptually, this assumes that RBCs are memory-less as they move through the network; the probability that a RBC moves into vessel v_{i+1} depends only on its current vessel v_i and not on any previous vessel. Using this simplification, the probability of the path under consideration now reads

$$\mathbb{P}(v_1, v_2, \dots, v_n) = \mathbb{P}(v_1) \prod_{i=1}^{n-1} \mathbb{P}(v_{i+1} \mid v_i). \quad (19)$$

The first term is unconditioned and simply represents the marginal probability that a RBC transits v_1 rather than some other inlet. This probability is therefore the ratio of the RBC flow in v_1 to the sum of RBC flow in all other inlet vessels,

$$\mathbb{P}(v_1) = \frac{|Q_{v_1}| H_{v_1}}{\sum_{v_i \in I} |Q_{v_i}| H_{v_i}}, \quad (20)$$

where I is the set of all inlet vessels.

The remaining terms take one of two forms. Imagine that vessels v_{i+1} and v'_{i+1} are the outflows of a diverging node with inflow vessel v_i . We assume that the probability that a RBC moves from v_i to v_{i+1} is simply the ratio of RBC flow in v_{i+1} to RBC flow in v_i ,

$$\mathbb{P}(v_{i+1} \mid v_i) = \frac{|Q_{v_{i+1}}| H_{v_{i+1}}}{|Q_{v_i}| H_{v_i}}, \quad (21)$$

and similarly for the probability that a RBC moves from v_i to v'_{i+1} .

Alternatively, if instead v_{i+1} is the outflow of a converging node with inflows v_i and v'_i then,

$$\mathbb{P}(v_{i+1} \mid v_i) = 1, \quad (22)$$

that is, if a RBC is in vessel v_i , then it will surely go to vessel v_{i+1} , and similarly if a RBC is previously in vessel v'_i instead.

For a given equilibrium network configuration, we construct the global TTD in three steps:

1. Identify all paths through the network from any inlet to any outlet (*e.g.*, via a series of depth first searches initiated at each of the inlets of the network)
2. Compute the associated path probabilities by applying Equations 20 – 22 to Equation 19
3. Compute the associated path transit times,

$$\tau = \sum_{i=1}^n \frac{\pi L_i D_i^2}{4 \mid Q_i \mid}. \quad (23)$$

The resulting TTD is a discrete PDF with $P_T(T = \tau)$ equal to the sum of the probabilities (each given by Equation 19) of all paths that have transit time τ . Note that in networks with realistic geometries, each transit time will be associated with a unique path.

In order to put transit times in context and to facilitate comparisons between the TTDs of different flow configurations, we often normalize transit times, either by the bulk transit time, V/Q ,

$$\hat{\tau} = \tau Q/V, \quad (24)$$

where $V = \sum_{i=1}^{N_v} \pi \ell_i d_i^2/4$ is the total volume of the network and Q is the total volumetric flow rate entering the network, or by the mean transit time

$$\bar{\tau} = \sum_{p \in \mathcal{P}} \mathbb{P}_T(\tau_p) \tau_p, \quad (25)$$

where \mathcal{P} is the set of all flow pathways through the network. Note that in general the bulk transit time is not equal to the expected transit time.

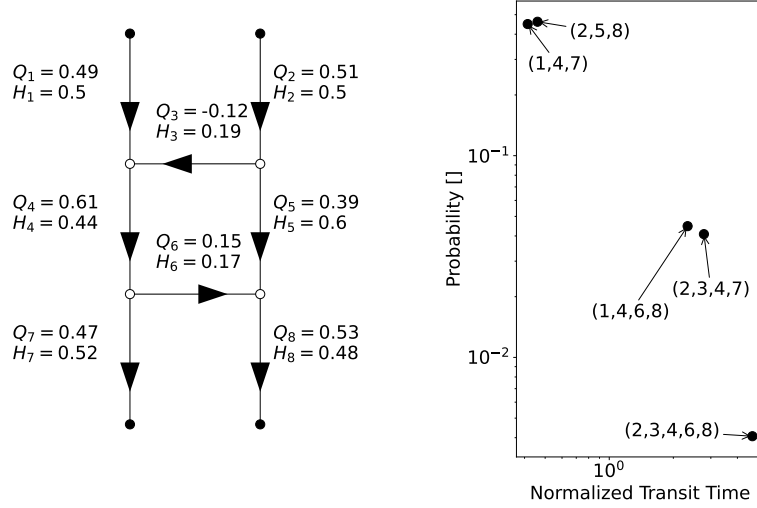


Figure 3: An equilibrium flow configuration of the two-rung ladder network (left) and its TTD (right). Each atom in the TTD corresponds to a flow pathway through the network. Transit time for each path is normalized by bulk transit time.

2.5. Example: Two-Rung Ladder Network

For a simple expository case, we consider the two-rung ladder as seen in the left pane of Figure 3. Here, we set pressures $P_1 = 1$, $P_2 = 1.01$ and $P_7 = P_8 = 0$ so that in general flow proceeds top to bottom, and inlet hematocrits at node 1 and node 2 in this example are identical and equal to 0.5. All vessel lengths and diameters are equal, except for the rungs (vessels 3 and 6) which have double the diameter of other vessels in the network.

This equilibrium flow configuration supports 5 distinct flow pathways, which we list by vessel: $(1,4,7)$, $(2,5,8)$, $(1,4,6,8)$, $(2,3,4,7)$ and $(2,3,4,6,8)$. We compute the transit time associated with each path according to Equation 23. For the longest path in this flow configuration, $(2,3,4,6,8)$, we find that

$$\tau = \frac{\pi d^2 \ell}{4} (Q_2^{-1} + 4|Q_3|^{-1} + Q_4^{-1} + 4Q_6^{-1} + Q_8^{-1}), \quad (26)$$

$$\Rightarrow \hat{\tau} \approx 4.70. \quad (27)$$

Thus, the transit time for this path is almost five times the bulk transit time.

We can derive the probability that an incoming RBC travels along this path using Equations 19 – 22. The probability a RBC transiting the inlet 2

is

$$P(v_2) = \frac{Q_2 H_2}{Q_1 H_1 + Q_2 H_2} \quad (28)$$

As the next node encountered along the path is diverging, the conditional probability of a RBC transiting vessel 3 given it is in vessel 2 is then

$$P(v_3 | v_2) = \frac{|Q_3| H_3}{Q_2 H_2} \quad (29)$$

The following node in the path is converging, and so the conditional probability of a RBC transiting vessel 4 given it has transited vessel 3 is

$$P(v_4 | v_3) = 1 \quad (30)$$

Again, we encounter a diverging node, giving a conditional probability similar to before:

$$P(v_6 | v_4) = \frac{|Q_6| H_6}{Q_4 H_4} \quad (31)$$

The final interior node in the sequence is converging, giving

$$P(v_8 | v_6) = 1 \quad (32)$$

The overall probability is the product of these

$$P_T(\tau) = \left(\frac{Q_2 H_2}{Q_1 H_1 + Q_2 H_2} \right) \left(\frac{|Q_3| H_3}{Q_2 H_2} \right) (1) \left(\frac{|Q_6| H_6}{Q_4 H_4} \right) (1) \quad (33)$$

$$\approx 0.004, \quad (34)$$

i.e., there is a roughly 0.4% that an incoming RBC will travel along this path. Repeating this procedure for all flow pathways generates the full TTD, as seen in the right pane of Figure 3. Notice that roughly 90 percent of all RBCs entering the network flow along one of two dominant paths that do not involve the rungs of the ladder. Almost all of the remaining 10 percent of RBCs transit just one of the two rungs.

Under the prescribed boundary conditions, this network supports equilibrium flow configurations for left-to-right, right-to-left, and approximately zero flow in each of the rungs, leading to 9 distinct equilibria, and each equilibrium has its own TTD. The PDFs of these TTDs are featured in Figure 4; the equilibria we previous considered is featured in the top left pane. Plotting individual PDFs will become cumbersome as the number of equilibria supported by the network grows, and so we often opt instead to plot CDFs.

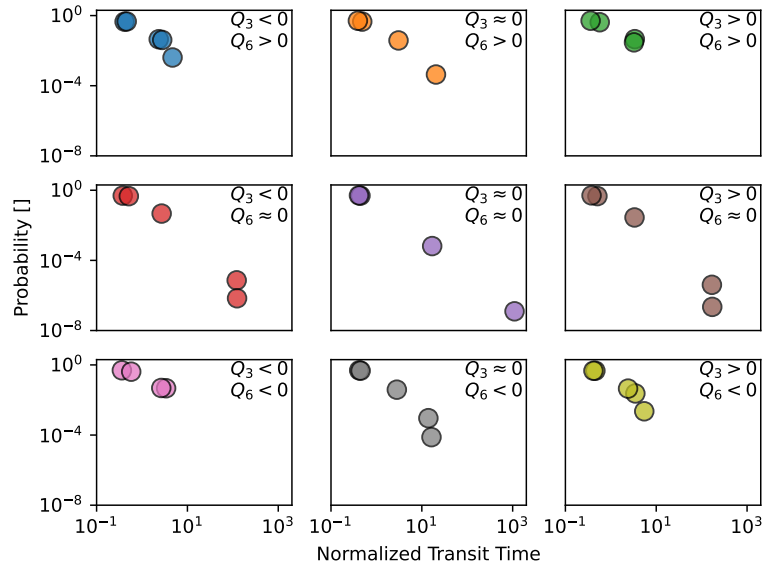


Figure 4: Probability density functions of the transit time distributions for all 9 equilibria supported by the 2-rung ladder network. Transit times have been normalized by bulk transit time.

2.6. Honeycomb Networks

We apply the methods described in this section to the regular and perturbed honeycomb networks seen in the left and right panes in Figure 5, respectively. In the regular network, all diameters are equal, whereas in the perturbed network, we apply a $\pm 10\%$ perturbation. In both networks, we set pressure boundary conditions of $P = 1$ at all exterior nodes at the top of the network and $P = 0$ at all exterior nodes at the bottom of the network. We enforce hematocrit of 0.45 at each inlet, and use $p = 2$ in the plasma skimming function from Equation 2. In both networks, we apply periodic boundary conditions in the horizontal direction, so edges wrap from the left side to the right side of the schematics in Figure 5.

For each network, we sample 1000 hematocrit profiles uniformly randomly from $[0, 1]^{N_v}$ as initial conditions for Equation 16. We attempt to find a solution using the nonlinear root finder from `scipy.optimize.fsolve`. If the solver is successful, we store the solution for further analysis. Due to possible numerical imprecision in these solutions, we will present here only equilibria that differ in at least one flow direction from every other equilibrium in the collection, thus guaranteeing that we are not over-representing the total number of equilibria supported by each network type.

3. Results

Of the 1000 total attempts, we find 1000 distinct equilibria in the regular honeycomb network and 462 distinct equilibria in the perturbed honeycomb network. These equilibrium configurations can be analyzed either singularly or en masse.

For a single equilibrium for each network type, we can analyze normalized flow distribution and hematocrit distribution as in Figure 6. Each mark in this visualization represents a vessel in the network. The joint distribution shows clear structure. The gray reference curve represents vessels that have RBC flow equal to the inlet RBC flow, i.e. $HQ = H_{in}Q_{in}$. For this equilibrium we have $H_{in} = 0.45$ and assume $Q_{in} = 1/6$ at each inlet, so that $H = 0.075/Q$ along this arc. The gray reference ray represents the linear approximation of plasma skimming at low relative flow rates, $H = (p - 1)H_{in}Q/Q_{in} = 2.7Q$.

Each equilibrium in the collection has its own MCTT and CTTH, and so when we look across all detected equilibria, we arrive at *distributions* of MCTT and CTTH, as seen in Figure 7. Each mark in this visualization

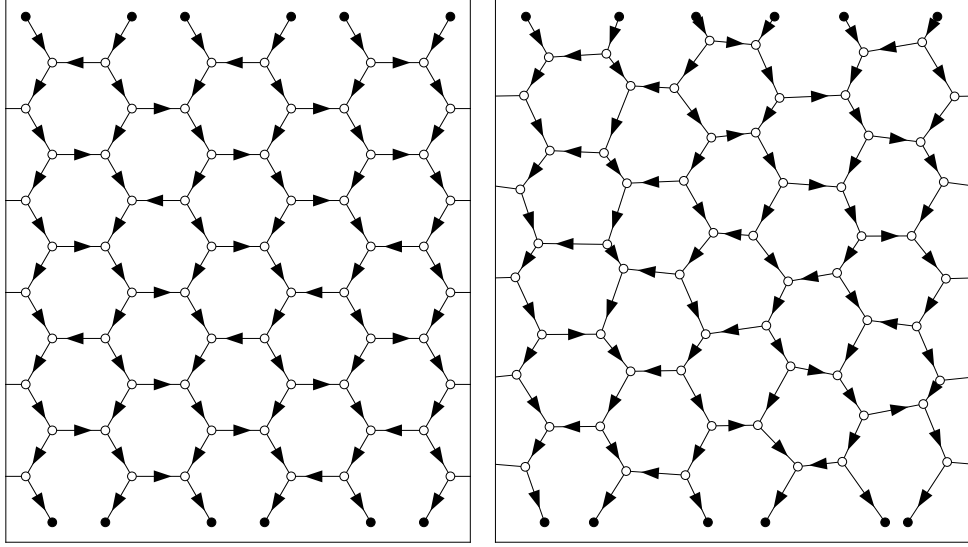


Figure 5: Regular honeycomb (left) and perturbed honeycomb (right) networks. Black nodes are exterior, and white nodes are interior. Arrows indicate flow direction in a particular equilibrium network configuration.

represents a distinct equilibrium. Note that the units of both MCTT and CTTH in this figure are arbitrary but are mutually consistent; multiplicatively scaling all diameters and/or lengths and/or pressures would result in simple rescaling of the horizontal and vertical axes but would not change any of the substantive conclusions of the analysis. Reference lines represent constant ratio of CTTH to MCTT (that is, constant coefficient of variation for the TTD), ranging from 1 (top ray) to 0.1 (bottom ray). This is not to be confused with the slope of the each point cloud, which provides information about the relative sensitivities of MCTT and CTTH to the introduction of long-delay flow pathways and/or additional RBC recruitment to existing long-delay flow pathways. Note that both these rays and the overall slopes of the point clouds are independent of network scaling.

In Figure 8 and Figure 9, we see the full collection of TTD CDFs for both network types. The bars in Figure 8 contain 80% of observed TTDs at the associated probability; a similar interpretation holds true for 9. Note that these bars are *not* confidence intervals in the inferential statistics sense, but instead are simply intended to give a sense of the spread of TTD observations

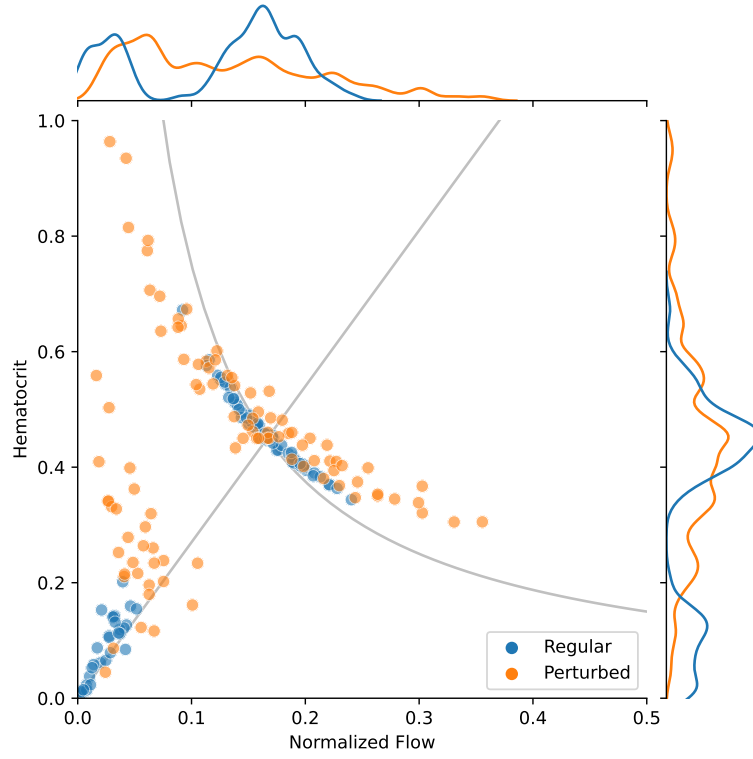


Figure 6: Joint distribution of normalized flow and hematocrit at an arbitrarily chosen equilibrium for both the regular and perturbed network. Each mark here represents a vessel in the respective network. Marginal plots represent kernel density estimates of the marginal distributions of each network type. The reference arc represents complete RBC conservation from source to sink, and the reference ray represents the linear approximation of plasma skimming for low flow rates.

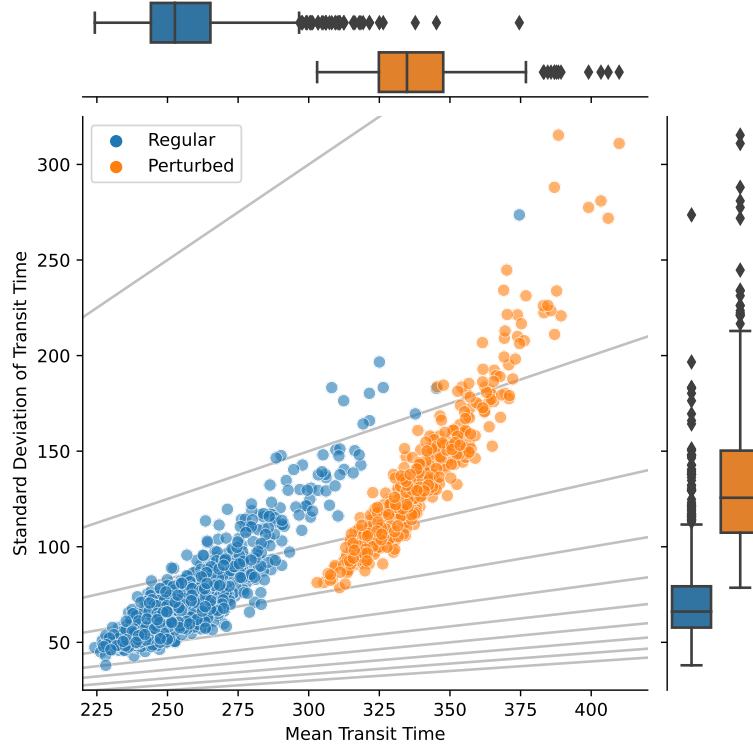


Figure 7: Joint distribution of mean and standard deviation (arbitrary units) of the TTDs associated with the regular and perturbed networks. Each mark here represents a distinct equilibrium. Marginal plots represent standard boxplots of the marginal distributions of each network type. Reference rays represent constant coefficient of variation of the TTD, ranging from 1 (top ray) to 0.1 (bottom ray) in steps of 0.1.

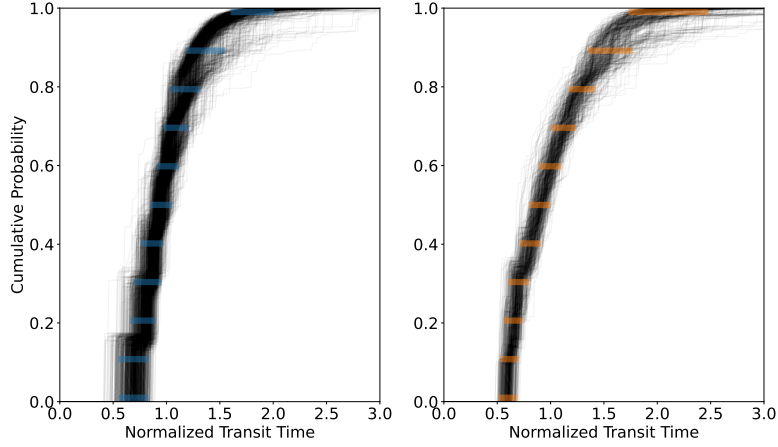


Figure 8: Collection of TTD CDFs for each equilibria identified in the regular (left) and perturbed (right) honeycomb network. Orange bars contain 80% of TTDs at the associated cumulative probability. Transit times have been normalized by the mean transit time.

at various points.

In Figure 8, we see that at low to moderate cumulative probabilities, TTDs exhibit a greater spread in the regular network than in the perturbed network. At high cumulative probabilities, this observation is reversed: TTDs exhibit a significantly smaller spread in the regular network than in the perturbed network. We see a similar outcome in Figure 9: at low to moderate normalized transit times, TTDs exhibit a greater spread in the regular network than in the perturbed network, and the opposite at high normalized transit times.

4. Discussion

The simple 2-rung ladder network presented in Section 2 supported 9 distinct equilibria; flow in each rung could be right-to-left, left-to-right, or approximately zero. Extending this same logic, generalized ladder networks with n rungs, equal diameters, and symmetric boundary conditions may support 3^n distinct equilibria. Each “column” of the honeycomb networks seen in Figure 5 is a 5-rung ladder, with adjacent ladders offset from one another to ensure all nodes connect three vessels rather than four. With 5 rungs in each of 6 columns (including the wrapped edges) in the networks considered here, the regular network might support up to $3^{30} \approx 2 \times 10^{14}$ distinct equilibrium states. It is perhaps not surprising then that *all* of the

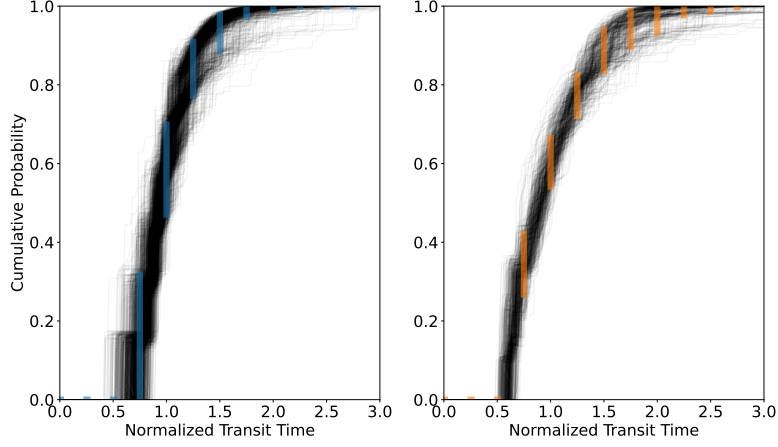


Figure 9: Collection of TTD CDFs for each equilibria identified in the regular (left) and perturbed (right) honeycomb network. Orange bars contain 80% of TTDs at the associated normalized transit time. Transit times have been normalized by the mean transit time.

1000 initial hematocrit profiles resulted in a distinct equilibrium. Moreover, this diversity of equilibrium configurations is resilient to perturbations to vessel lengths and diameters; nearly half of the initial conditions resulted in distinct equilibria in the perturbed network.

It is often analytically convenient to assume simple closed form approximations for the distribution of flows at steady state [3], but Figure 6 shows that some caution is needed in generalizing this approach to all network topologies. Note that in regular networks, both flow and hematocrit are strongly bimodal whereas in perturbed networks, this bimodal character is significantly dampened. The bimodal nature of the flow and hematocrit in regular networks is due to the difference between the rails and the rungs of the ladder: the rungs tend to have low flow rates and correspondingly low hematocrit values (points close to the origin), while the rails carry almost all of the incoming RBC flow (points close to the reference curve). For the rails, plasma-skimming ensures that RBCs will be divided between daughter vessels, with some vessels being enriched in hematocrit (marks directly above the reference arc) and some vessels being depleted (marks directly below the reference arc). Both enrichment and depletion are mediated by the rungs of the honeycomb, and in these vessels hematocrit is roughly linear in the flow, which according to the plasma-skimming function would be $H \approx (p - 1)H_{in}Q/Q_{in} = 2.7Q$. Breaking the regular symmetry starts to

blur the distinction between rails and rungs.

Both distributions feature spread of vessel hematocrits about the fixed inlet hematocrit of 0.45, but notice, too, that some vessels in the perturbed network have hematocrit near 1. This is due to the so-called *pathway effect* in which hematocrit is progressively enriched along a series of diverging bifurcations. This emphasizes the importance of either considering small to medium networks (like the ones presented here) or using plasma skimming functions that are parameterized by feed hematocrit and are well calibrated to high hematocrit scenarios (unlike the one used here). Note that while we plot here the flow and hematocrit distributions for a single arbitrarily chosen equilibrium for each network type, the results presented here are broadly consistent across all equilibria we inspected.

Previous work has assumed (often tacitly) that a *network* exhibited a particular mean capillary transit time (MCTT) and capillary transit time heterogeneity (CTTH), but Figure 7 shows that this approach is misguided. In the regular network, half of all detected equilibria have MCTT between roughly 244 and 265, with a median MCTT of 253. Note that there is considerable spread among larger MCTTs in this network type. That is, while most detected equilibria are relatively similar in the types of flow pathways they support, it is relatively easy to configure the network in such a way that at equilibrium it supports highly subscribed, long-delay flow pathways. The major differentiation of the perturbed network is the central tendency of MCTT, not its variability. Half of detected equilibria now have MCTT between 325 and 348, with a median MCTT of 335 – the interquartile range remains largely unchanged compared to the regular network, but the median MCTT has shifted considerably.

A similar pattern plays out in CTTH. The equilibria of the regular network are quite similar to one another with respect to CTTH. That is not to say the the RBCs flowing in any one particular equilibrium network configuration experience very similar transit times, but instead whatever variability these RBCs *do* experience in transit time is roughly consistent across different equilibrium configurations. Taken across all detected equilibria, CTTH tends to be both higher and more variable in the perturbed network – there is both greater variability of RBC transit times *within* a particular equilibrium network configuration and larger differences in CTTH *between* different equilibria.

The point clouds of both network types are approximately linear. Moreover, CTTH is more sensitive to changes in MCTT in the perturbed network

than in the regular network; the OLS slopes of best fit are 1.14 and 1.92 for the regular and perturbed point clouds, respectively. That is not to say that MCTT itself is directly driving changes in CTTH, but instead that the introduction of longer delay flow pathways or increases in capillary recruitment along existing long delay flow pathways affects CTTH more strongly than MCTT in both networks, and affects CTTH more strongly in the perturbed network than in the regular network.

Whenever we consider changes in variability, it is both convenient and informative to place these in context. Here, we take a traditional approach and compare standard deviation to the mean by computing the coefficient of variation $CTTH/MCTT$; the reference rays in Figure 7 represent different coefficients of variation, ranging from 1 (top ray) to 0.1 (bottom ray) in steps of 0.1. Note that the vast majority of equilibria in the regular network have coefficients of variation between 0.6 and 0.8, while most equilibria of the perturbed network have coefficients of variation between 0.7 and 0.9.

The method proposed here allow us to move beyond a discussion of first and second moments of TTDs and towards a more general understanding of the diversity of TTDs a network might exhibit. In both Figure 8 and Figure 9, we see the TTD CDFs for all detected equilibria for each network type. The diversity of these TTDs can be quantified in two primary ways: variability in transit time for a given cumulative probability (Figure 8) and variability in cumulative probability for a given transit time (Figure 9). The former is essentially a method of uncertainty analysis on the percentiles of the TTD; in Figure 8, we show (approximate) deciles as a use case. Orange bars contain 80% of TTDs at the associated probability. For instance, in 80% of detected equilibria, the quickest 10% of RBCs to exit the regular network (bottom bar in left pane of Figure 8) so after a normalized transit time of 0.58 to 0.80. The equivalent range in the perturbed network is considerably narrower – just 0.56 to 0.67 normalized transit times. This trend continues through most of the deciles; only among the slowest RBCs to exit the network does the perturbed network show more variability than the regular network. In 80% of detected equilibria, the slowest 1% of RBCs to exit the regular network (top bar, left pane, Figure 8) do so between 1.60 to 1.98 normalized transit times after entering the network. The equivalent range for the perturbed network is 1.76 to 2.45. We conclude that when taken over all detected equilibria, the slowest RBCs in the perturbed network both tend to stay in the network longer and to have more variability in their transit time than their peers in the regular network.

In Figure 9 we see the same collection of TTD CDFs with different contextual data. Bars contain 80% of the TTDs at the associated transit time, shown here at intervals 0.25 normalized transit times. We would expect between 0% and 32% of the RBCs the regular network to have transited the network within 0.75 normalized transit times. The perturbed network will likely have cleared between 27% and 42% of RBCs within the same time frame. Thus, among RBCs with lower transit times, the perturbed network clears a larger proportion of RBCs (and with less variability) than its regular counterpart. This relationship continues until roughly 1.5 normalized transit times: after waiting 1.5 normalized transit times, we would expect the regular network to have cleared between 89% and 98% of RBCs, where as the perturbed network will typically have cleared between 84% and 94%.

5. Conclusion

We present a methodology for identifying a large number of distinct equilibria in two flavors of honeycomb network and computing an approximate transit time distribution for each. This collection of TTDs contains a wealth of information that can be examined in several distinct and equally informative manners.

In presenting our specific networks and particular pieces of analysis, we do not mean to intend to imply that these are the *only* features in which one might be interested. At the same time, minor modifications of these ideas can cover a wide range of applications, including quantifying the likelihood that a RBC will exit the capillary bed before exhausting its oxygen payload and the likelihood that a RBC will remain in the network after becoming unable to deliver oxygen effectively. Moreover, we can concretely quantify the uncertainty inherent in these estimates given the presence of multiple steady-state configurations in the network and compare both these estimates and their uncertainty between different networks, *e.g.*, between capillary networks in different tissue types, between cancerous and non-cancerous morphologies of the capillary networks in the same tissue type, or between networks before and after a physiological change to the capillary bed like vessel dilation or angiogenesis.

The method presented is open to improvement. As we noted previously, without incorporating more physiologically relevant plasma skimming laws – particularly those that have been well calibrated to high feed hematocrit scenarios – network size will be effectively limited due to the pathway effect.

When computing the conditional probabilities used to approximate the TTD, we made a Markovian assumption – RBCs do not “remember” their entire path through the network. And yet know from experimental evidence that this assumption is flawed for many network topologies and under many flow conditions. Incorporating a more detailed and accurate description of the down-stream consequences of up-stream “decisions” by RBCs may well be critical for creating accurate TTD approximations in some networks.

6. Code & Date

Python notebooks for data generation and figure creation can be found at <https://github.com/NathanKarst/NetworkTransitTimes>.

7. Acknowledgments

The authors would like to thank Gwennou Coupier and Thomas Podgorski for helpful exploratory conversations early in this work.

References

- [1] Ostergaard, L. *Blood flow, capillary transit times, and tissue oxygenation: the centennial of capillary recruitment*. Journal of Applied Physiology, 192(6):1413–1421.
- [2] Jespersen, S. N., & Østergaard, L. (2012). *The roles of cerebral blood flow, capillary transit time heterogeneity, and oxygen tension in brain oxygenation and metabolism*. Journal of cerebral blood flow and metabolism, 32(2), 264–277.
- [3] Goirand, F., Le Borgne, T. & Lorthois, S. (2021). *Network-driven anomalous transport is a fundamental component of brain microvascular dysfunction*. Nature Communications 12, 7295.
- [4] Ostergaard, L., Kristiansen, S. B., Angleys, H., Frøkiær, J., Michael Hasenkam, J., Jespersen, S. N., & Bøtker, H. E. (2014). *The role of capillary transit time heterogeneity in myocardial oxygenation and ischemic heart disease*. Basic research in cardiology, 109(3), 409.

- [5] Lückner, A., Secomb, T. W., Weber, B., & Jenny, P. (2018). *The Relation Between Capillary Transit Times and Hemoglobin Saturation Heterogeneity. Part 1: Theoretical Models*. *Frontiers in Physiology* 9
- [6] Lückner, A., Secomb, T. W., Barrett, M. J. P., Weber, B., & Jenny, P. (2018). *The Relation Between Capillary Transit Times and Hemoglobin Saturation Heterogeneity. Part 2: Capillary Networks*. *Frontiers in Physiology* 9
- [7] Ahuja, R., Magnanti, T & Orlin, J. (1993) *Network Flows: Theory, Algorithms, and Applications*. Pearson.
- [8] Gardner, D., Li, Y., Small, B., Geddes, J.B., & Carr, R.T. (2010) *Multiple Equilibrium States in a Micro-vascular Network*. *Mathematical Biosciences* 227:117–124
- [9] Karst, N. J., Geddes, J. B., & Carr, R. T. (2017) *Model Microvascular Networks Can Have Many Equilibria*. *Bulletin of Mathematical Biology* 79:662–681
- [10] Geddes, J. B., Storey, B. D., Gardner, D., & Carr, R. T. (2010) *Bistability in a Simple Fluid Network Due to Viscosity Contrast*. *Phys Rev E* 81:046316
- [11] Tawfik Y, Owens RG (2013) *A Mathematical and Numerical Investigation of the Hemodynamical Origins of Oscillations in Microvascular Networks*. *Bulletin of Mathematical Biology* 75(4):676–707
- [12] Davis JM, Pozrikidis C (2010) *Numerical Simulation of Unsteady Blood Flow through Capillary Networks*. *Bulletin of Mathematical Biology* 73(8):1857–1880
- [13] Davis JM (2014) *On the Linear Stability of Blood Flow Through Model Capillary Networks*. *Bulletin of Mathematical Biology* 76(12):2985–3015
- [14] Davis JM, Pozrikidis C (2014) *Self-sustained Oscillations in Blood Flow Through a Honeycomb Capillary Network*. *Bulletin of Mathematical Biology* 76(9):2217–2237
- [15] Carr RT, Lacoïn M (2000) *Nonlinear Dynamics of Microvascular Blood Flow*. *Annals of Biomedical Engineering* 28(6):641–652

- [16] Carr RT, Geddes JB, Wu F (2005) *Oscillations in a Simple Microvascular Network*. Annals of Biomedical Engineering 33(6):764–771
- [17] Geddes JB, Carr RT, Karst N, Wu F (2007) *The Onset of Oscillations in Microvascular Blood Flow*. SIAM Journal on Applied Dynamical Systems 6(4): 694–727
- [18] Karst NJ, Storey BD, Geddes JB (2015) *Oscillations and Multiple Equilibria in Microvascular Blood Flow*. Bulletin of Mathematical Biology 77:1–24
- [19] Ben-Ami, Y., Atkinson, G. W., Pitt-Francis, J. M., Maini, P. K. & Byrne, H. M. (2022) *Structural Features of Microvascular Networks Trigger Blood Flow Oscillations* Bulletin of Mathematical Biology 84:85
- [20] Huang, W., Shi, J., & Yen, R. T. (2012). Stochastic simulation of human pulmonary blood flow and transit time frequency distribution based on anatomic and elasticity data. Molecular & cellular biomechanics : MCB, 9(4), 269–283.
- [21] Huang W, Yen RT, McLaurine M, Bledsoe G. (1996) *Morphometry of the human pulmonary vasculature*. J Appl Physiol 81(5):2123-33. .
- [22] Chiba A, Suzuki OY, Nakanishi H, Chichibu S (1998) *Gastric vascular network in stroke-prone spontaneously hypertensive rats*. Research Communications in Molecular Pathology and Pharmacology 100:65–76
- [23] Dunlop SA, Moore SR, Beazley LD (1997) *Changing patterns of vasculature in the developing amphibian retina*. Journal of Experimental Biology 200:2479–2492.
- [24] Lauwers F, Sassot F, Lauwers-Cances V, Puwanarajah P, Duvernoy H (2008) *Morphometry of the human cerebral cortex microcirculation: general characteristics and space-related profiles*. Neuroimage 39:936–948
- [25] Ribatti D (2008) *Chick embryo chorioallantoic membrane as a useful tool to study angiogenesis*. International Review of Cell and Molecular Biology 270:181–224

- [26] Pries AR, Fritzsche A, Ley K, Gaehtgens P (1992) *Redistribution of Red Blood Cell Flow in Microcirculatory Networks by Hemodilution*. Circulation Research
- [27] Pries AR, Secomb TW, Gaehtgens P, Gross JF (1990) *Blood flow in microvascular networks. Experiments and simulation*. Circulation Research 67(4):826–834
- [28] Klitzman B, Johnson PC (1982) *Capillary Network Geometry and Red Cell Distribution in Hamster Cremaster Muscle*. American Journal of Physiology 242(2):H211–H219